

# Neighborhood Feature Pooling for Remote Sensing Image Classification

Fahimeh Orvati Nia<sup>1</sup>, Amirmohammad Mohammadi<sup>1</sup>, Salim Al Kharsa<sup>1</sup>, Pragati Naikare<sup>2</sup>,  
Zigfried Hampel–Arias<sup>1,3</sup>, and Joshua Peebles<sup>1,3</sup>

<sup>1</sup>Dept. of Electrical & Computer Engineering, Texas A&M University, College Station, TX, USA

<sup>2</sup>Dept. of Computer Science & Engineering, Texas A&M University, College Station, TX, USA

<sup>3</sup>Los Alamos National Laboratory, Los Alamos, NM, USA

## Abstract

*In this work, we propose neighborhood feature pooling (NFP) as a novel texture feature extraction method for remote sensing image classification. The NFP layer captures relationships between neighboring inputs and efficiently aggregates local similarities across feature dimensions. This new approach is implemented using convolutional layers and can be seamlessly integrated into any network. Results comparing the baseline models and the NFP method indicate the potential of this new approach for classification. NFP consistently improves performance across diverse datasets and architectures while maintaining minimal parameter overhead. The code for this work is publicly available.<sup>1</sup>*

## 1. Introduction

Remote sensing has various applications in environmental monitoring [12], urban planning [25], and agriculture [16]. Machine learning, particularly convolutional neural networks (CNNs), has been used in processing and analyzing remote sensing images [13, 32]. In high-resolution remote sensing imagery, fine-grained textural patterns can often distinguish different land-cover or scene types [20]. For example, in the University of California Merced (UCMerced) Land Use dataset [30] and the Northwestern Polytechnical University-Remote Sensing Image Scene Classification (NWPU-RESISC45) benchmark [3], visual distinctions between categories often lie in recurrent textures or spatial arrangements (*e.g.*, the grid-like layout of residential blocks versus the irregular granular pattern of forest canopies) rather than unique objects [4].

However, standard CNN architectures can inadvertently lose these cues when using traditional pooling operations

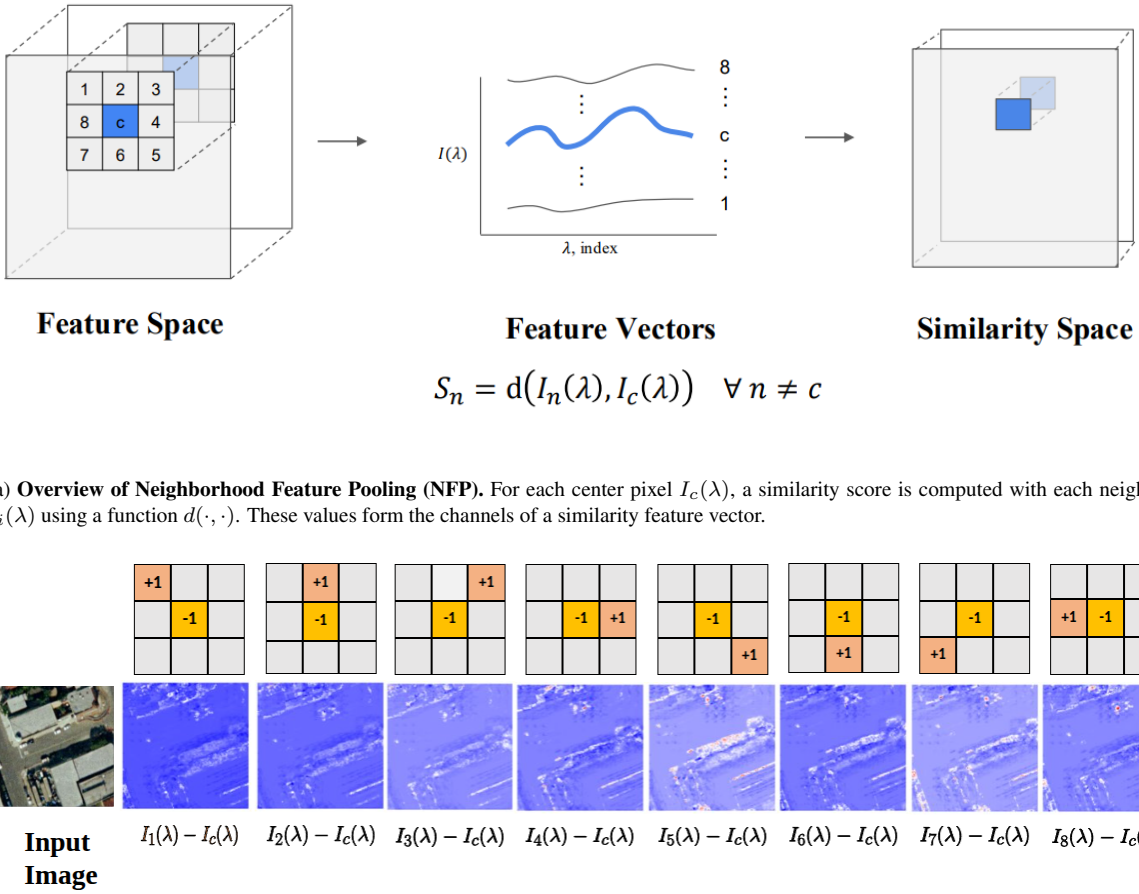
(e.g., average and max pooling). These layers are effective in summarizing information at reduced spatial dimensions, yet typically fail to encode important structural details [33]. This limitation stems from the lack of explicit weighting on neighboring relationships within the feature space. To address this gap, neighborhood feature pooling (NFP) is introduced in this work. This is a novel layer that measures how similar each neighbor is to a center pixel and/or feature vector. NFP can work alongside the usual global average pooling (GAP), adding a texture-aware branch for improved feature representation.

## 2. Related Work

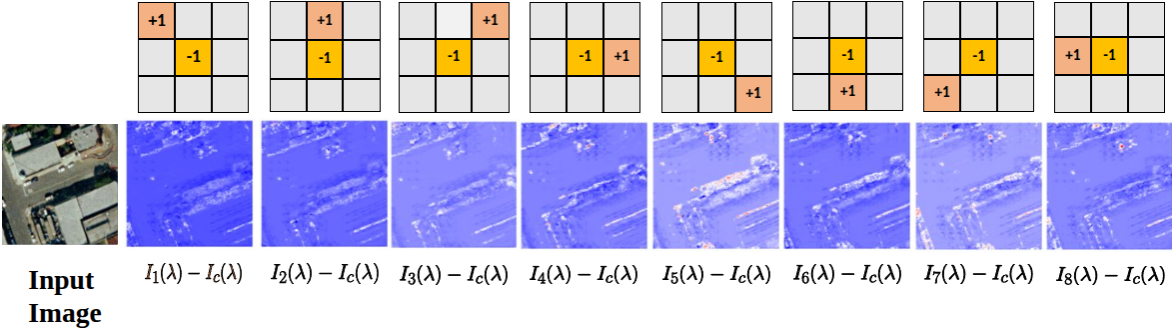
Several methods have been proposed to address the challenge of encoding structural detail for texture recognition. For example, Local Binary Patterns (LBP) [18] capture texture information by encoding the difference in the center pixel between each of its neighbors and computing a weighted sum based on the binary position of the neighboring pixel. However, LBP operates on grayscale intensities and discards magnitude information [1], limiting its ability to encode fine variations in images. Several advanced texture encoding and pooling methods have been proposed to improve texture representation. Deep Texture Encoding Network (DeepTEN) [31] leveraged dictionary learning to encode texture information in learnable codewords that captured robust features. Randomized Deep Activation Map pooling (RADAM) [22] samples and aggregates deep activation maps in a randomized manner to capture a wide range of texture patterns via stochastic encoding. Fractal-based pooling techniques, including implementations based on lacunarity [7, 15], quantify texture complexity at multiple scales by analyzing the distribution of gaps in local pixel density across spatial patterns.

Texture descriptors in images may be statistical, summarizing pixel-value distributions, or structural, modeling relationships among neighboring pixels [19]. Two recent structural approaches exploit similarity maps to enrich con-

<sup>1</sup>[https://github.com/Advanced-Vision-and-Learning-Lab/Neighbour\\_Feature\\_Pooling](https://github.com/Advanced-Vision-and-Learning-Lab/Neighbour_Feature_Pooling)



(a) **Overview of Neighborhood Feature Pooling (NFP).** For each center pixel  $I_c(\lambda)$ , a similarity score is computed with each neighbor  $I_i(\lambda)$  using a function  $d(\cdot, \cdot)$ . These values form the channels of a similarity feature vector.



(b) Detailed illustration of NFP with  $r = 1$ . An input patch from the UC Merced dataset (“buildings” class) is processed with eight directional difference kernels, which measure relative feature differences between the center pixel and its neighbors (scaled dot product Similarity). For visualization, the outputs are normalized to the range  $[0,1]$  and computed with a dilation factor of 15, yielding NFP maps that form a multi-channel similarity representation of local texture relationships, later aggregated into the NFP feature vector.

Figure 1. NFP illustration. (a) Overview of the Neighborhood Feature Pooling framework. (b) Example with  $r = 1$ , showing the input patch, directional kernels, and the resulting similarity maps that encode local texture relationships. Together these demonstrate how NFP captures local structural information that is later integrated with global features (Fig. 2).

volutional features. The Local Similarity Pattern (LSP) layer appends cosine-similarity maps between each pixel and its eight-neighbor window, supplying additional structural cues for stereo-matching networks [14]. In multi-sensor anomalous change detection, a Neighborhood Similarity Feature Space (NSFS) concatenates dot-product similarity responses as extra channels, boosting texture discrimination without resampling [9]. While these methods demonstrate the benefit of neighbor-wise similarity, they employ fixed similarity metrics and rely on pooling operations that can reduce fine-grained texture patterns.

These advances highlight the importance of neighborhood similarity for texture encoding, but current methods remain constrained by handcrafted descriptors, fixed similarity choices, or stochastic sampling. This motivates our proposed Neighborhood Feature Pooling (NFP), which in-

tegrates learnable similarity maps directly into the backbone for end-to-end optimization with minimal parameter overhead.

### 3. Method

#### 3.1. Neighborhood Similarity Computation

The core operation of NFP involves comparing each center pixel with its surrounding neighbors using a feature-space similarity function. Let  $I_n(\lambda) \in \mathbb{R}^d$  denote the feature vector of a pixel at spatial position  $n$ , where  $\lambda \in \{1, \dots, d\}$  indexes the feature dimension. For a neighborhood of radius  $r$  centered at position  $c$ , the similarity  $S_n$  between the center  $I_c(\lambda)$  and each neighbor  $I_n(\lambda)$  is defined as

$$S_n = d(I_n(\lambda), I_c(\lambda)), \quad \forall n \neq c, \quad (1)$$

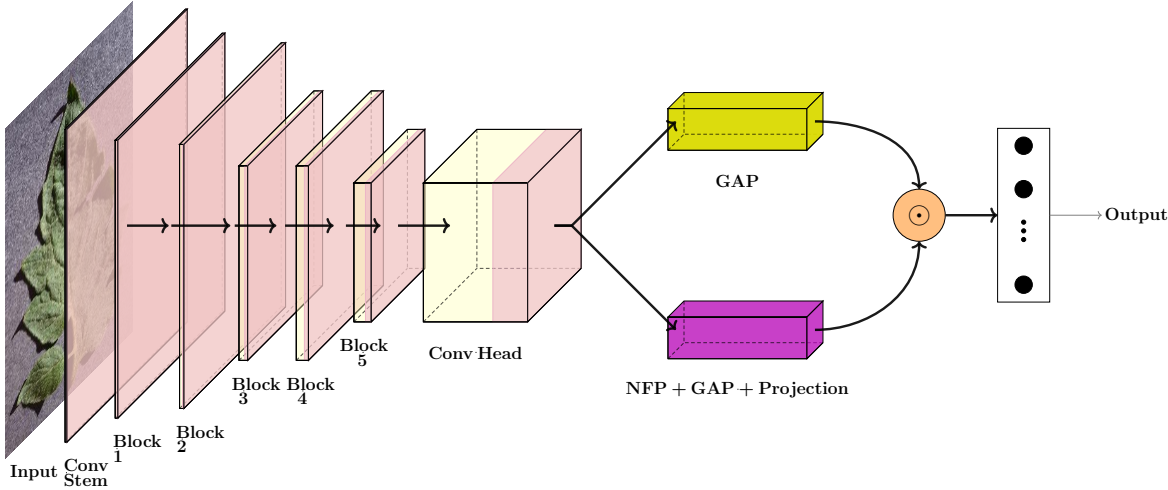


Figure 2. Full architecture illustration of the proposed model using MobileNetV3 [10] with NFP. Each block represents a stage in the feature extraction pipeline. After feature maps are extracted from the input, the features are aggregated through two branches: global average pooling (GAP) and NFP. The NFP branch first extract the similarity maps then the similarity values are aggregated through GAP. The average NFP features are then upsampled to the same dimension using a  $1 \times 1$  convolution. The final step is for the GAP and NFP feature vectors to be multiplied before being passed into the output classification layer.

where  $d(\cdot, \cdot)$  is a similarity function such as cosine or dot product. This operation yields a set of  $(2r + 1)^2 - 1$  scalar values per center pixel, producing a multi-channel similarity map that encodes local texture structure, as illustrated in Fig. 1.

Similarity measures such as cosine or Pearson correlation can yield negative values, which are retained to represent dissimilar or anti-correlated relationships between neighbors. For distance-based metrics such as  $L_p$  norm or RMSE, the computed distances are negated so that higher similarity consistently corresponds to larger values. This convention provides a unified interpretation across metrics and ensures that all similarity and distance functions are handled within a common framework.

In our experiments we fix  $r = 1$ , which results in 8 similarity values per feature channel. Larger neighborhoods could be used to capture broader spatial context at the expense of reduced boundary precision. The formulation in Eq. (1) thus provides an explicit mechanism for encoding relative feature-space relationships across local neighborhoods, preserving structural cues often discarded by global pooling.

### 3.2. Similarity Function Options

The similarity function  $d(\cdot, \cdot)$  in Eq. (1) can be drawn from a wide set of metrics, each emphasizing different aspects of feature space geometry. The choice of metric can influence NFP by defining how local neighborhood relationships are quantified. We follow the taxonomy of the first three categories defined by Deborah et al. [5] as the feature vectors are

similar to hyperspectral signatures used in remote sensing. We also introduced additional similarity metrics inspired by recent deep learning methods:

- **Category 1 (Vector in Euclidean space):**  $L_p$  norm, RMSE, Geman–McClure, Canberra, dot product (vanilla and scaled), cosine similarity, and sharpened cosine [28]
- **Category 2 ( $n$ -dimensional data in manifold):** Goodness-of-Fit Coefficient (GFC)
- **Category 3 (Distribution):** Chi-squared (two formulations), Hellinger, Jeffrey divergence, Squared-Chord, Pearson correlation, Smith’s measure, and Earth Mover’s Distance (EMD) [2].

This categorization preserves the theoretical grounding of [5] while covering all similarity measures implemented in the NFP module, ensuring both principled analysis and adaptability to modern feature representations. Cosine similarity is selected as the default due to its empirical performance across datasets. However, the modularity of NFP enables swapping any of the similarity functions, as further explored in Sec. 4.4.

### 3.3. Model Architecture Integration

As illustrated in Fig. 2, NFP is inserted after the final backbone stage and before the pooling/classification head. This configuration is used for all main results, while alternative placements (early-stage or multi-stage integration) are explored in Sec. 4.5. Given backbone feature maps  $X \in \mathbb{R}^{B \times C \times H \times W}$ , NFP constructs local neighborhoods of radius  $r$ , corresponding to a kernel size  $k = 2r + 1$  and

Backbone	Method	PlantVillage	RESISC45	UC Merced	GTOS-Mobile	EuroSAT
ResNet18	GAP	99.68 $\pm$ 0.07 (11.20)	91.28 $\pm$ 0.04 (11.20)	97.62 $\pm$ 0.19 (11.19)	72.01 $\pm$ 0.01 (11.19)	98.27 $\pm$ 0.19 (11.21)
	Lacunarity	99.73 $\pm$ 0.04 (11.20)	93.10 $\pm$ 0.01 (11.20)	97.30 $\pm$ 0.11 (11.19)	73.12 $\pm$ 3.21 (11.19)	98.23 $\pm$ 0.33 (11.21)
	Fractal	99.68 $\pm$ 0.03 (11.45)	92.29 $\pm$ 0.16 (11.47)	97.62 $\pm$ 0.34 (11.45)	69.43 $\pm$ 2.27 (11.46)	98.49 $\pm$ 0.20 (11.47)
	RADAM	99.61 $\pm$ 0.10 (11.20)	92.08 $\pm$ 0.15 (11.20)	97.46 $\pm$ 0.22 (11.20)	69.37 $\pm$ 2.68 (11.20)	98.40 $\pm$ 0.23 (11.21)
	DeepTEN	99.25 $\pm$ 0.05 (11.47)	93.19 $\pm$ 0.05 (11.96)	97.14 $\pm$ 0.58 (11.57)	71.66 $\pm$ 0.07 (11.73)	98.50 $\pm$ 0.28 (11.42)
	NFP (Ours)	<b>99.76 <math>\pm</math> 0.01</b> (11.23)	<b>93.22 <math>\pm</math> 0.25</b> (11.23)	<b>98.86 <math>\pm</math> 0.58</b> (11.23)	<b>74.52 <math>\pm</math> 0.02</b> (11.23)	<b>98.52 <math>\pm</math> 0.20</b> (11.26)
MobileNetV3	GAP	99.83 $\pm$ 0.04 (4.22)	94.48 $\pm$ 0.37 (4.23)	97.57 $\pm$ 0.57 (4.22)	76.27 $\pm$ 1.49 (4.23)	98.23 $\pm$ 0.13 (4.21)
	Lacunarity	99.82 $\pm$ 0.07 (4.22)	92.93 $\pm$ 0.41 (4.25)	97.94 $\pm$ 0.59 (4.23)	73.81 $\pm$ 0.26 (4.23)	98.52 $\pm$ 0.32 (4.21)
	Fractal	99.76 $\pm$ 0.11 (5.14)	93.55 $\pm$ 0.19 (5.17)	97.94 $\pm$ 0.22 (5.15)	75.46 $\pm$ 0.12 (5.15)	98.35 $\pm$ 0.15 (5.14)
	RADAM	99.45 $\pm$ 0.05 (4.22)	85.59 $\pm$ 2.61 (4.22)	97.78 $\pm$ 1.81 (4.22)	75.89 $\pm$ 3.58 (4.22)	98.27 $\pm$ 0.05 (4.21)
	DeepTEN	99.73 $\pm$ 0.08 (4.76)	<b>94.95 <math>\pm</math> 0.09</b> (5.68)	<b>98.49 <math>\pm</math> 0.31</b> (4.93)	<b>77.51 <math>\pm</math> 0.23</b> (5.25)	98.35 $\pm$ 0.23 (4.60)
	NFP (Ours)	<b>99.86 <math>\pm</math> 0.02</b> (4.31)	94.80 $\pm$ 0.21 (4.31)	<b>98.49 <math>\pm</math> 0.28</b> (4.31)	76.49 $\pm$ 1.17 (4.31)	<b>98.53 <math>\pm</math> 0.12</b> (4.30)
ViT-Tiny	GAP	<b>99.62 <math>\pm</math> 0.06</b> (5.53)	93.06 $\pm$ 0.49 (5.54)	97.78 $\pm$ 0.11 (5.53)	68.64 $\pm$ 3.75 (5.53)	<b>97.96 <math>\pm</math> 0.14</b> (5.53)
	Lacunarity	99.51 $\pm$ 0.04 (5.53)	<b>93.42 <math>\pm</math> 0.03</b> (5.54)	<b>97.86 <math>\pm</math> 0.19</b> (5.53)	74.71 $\pm$ 2.67 (5.53)	89.20 $\pm$ 0.36 (6.02)
	Fractal	<b>99.62 <math>\pm</math> 0.03</b> (5.57)	92.57 $\pm$ 0.61 (5.58)	<b>97.86 <math>\pm</math> 0.39</b> (5.57)	67.33 $\pm$ 0.78 (5.57)	92.47 $\pm$ 0.35 (6.05)
	RADAM	99.19 $\pm$ 0.29 (5.53)	91.75 $\pm$ 0.23 (5.53)	96.67 $\pm$ 0.89 (5.53)	67.68 $\pm$ 1.74 (5.53)	91.83 $\pm$ 1.21 (6.02)
	DeepTEN	99.25 $\pm$ 0.14 (5.64)	93.17 $\pm$ 0.09 (5.82)	97.62 $\pm$ 0.34 (5.67)	69.84 $\pm$ 2.66 (5.73)	88.42 $\pm$ 1.72 (6.09)
	NFP (Ours)	99.57 $\pm$ 0.07 (5.55)	92.79 $\pm$ 0.17 (5.55)	97.38 $\pm$ 0.34 (5.55)	<b>75.47 <math>\pm</math> 0.05</b> (5.55)	94.51 $\pm$ 0.88 (6.03)

Table 1. Classification accuracy (%) and model size (in millions of parameters) across five datasets using various texture pooling methods. Each cell shows Accuracy  $\pm$  Standard Deviation, followed by parameter count in parentheses. For each backbone architecture, the best-performing method on each dataset is highlighted in **bold**.

$N_r = k^2 - 1$  neighbors. Two depthwise (channel-wise) convolutions with fixed, sparse  $k \times k$  kernels are applied: one selects the center feature, while the other gathers the  $N_r$  neighbors. For distance-based variants, the kernel assigns +1 to the center and -1 to the neighbor. These operations produce an affinity stack  $S \in \mathbb{R}^{B \times N_r \times H' \times W'}$ , where  $H' = H - (k - 1)$  and  $W' = W - (k - 1)$ .

The affinity stack is spatially averaged and projected to a vector in  $\mathbb{R}^{C'}$  with  $C' = C$ . A  $1 \times 1$  convolution is applied only if  $C' \neq C$ . The resulting vector is fused with the backbone’s GAP representation via element-wise multiplication. Because both streams are pooled to vectors, the difference between  $(H, W)$  and  $(H', W')$  does not affect the fusion. This design preserves pretrained backbone weights and introduces only a lightweight projection layer as additional learnable overhead, making NFP broadly applicable across architectures such as ResNet, MobileNetV3, and ViT-Tiny, as detailed in Sec. 4.

## 4. Experiment

### 4.1. Experimental setup

Five public remote sensing datasets are used for evaluation: PlantVillage [11], UC Merced Land Use [30], RESISC45 [3], Ground Terrain in Outdoor Scenes (GTOS) Mobile [29], and EuroSAT. The first four datasets were RGB while EuroSAT was multi-spectral with 13 bands. PlantVillage is used with an 80/10/10 split, GTOS-Mobile follows the official split (84.5/9.4/6.1), and UC Merced, RESISC45, and EuroSAT follow the standard train/validation/test protocols

described by Neumann et al. [17]. To ensure fairness across baselines, all models are trained using identical data splits and preprocessing pipelines.

Experiments are run on a single NVIDIA A100 GPU using three random seeds to report mean and standard deviation. Training is performed for up to 100 epochs using the Adam optimizer with a learning rate of 0.001, a batch size of 32, and early stopping with a patience of 10 epochs. All images are resized to 256  $\times$  256. Training-time augmentations include horizontal and vertical flips, random rotations ( $\pm 15^\circ$ ), color jitter, and normalization (ImageNet statistics for RGB datasets and per-band statistics for multi-spectral EuroSAT, following [8]). At test time, only resizing and the same normalization are applied.

### 4.2. Backbone Networks

The NFP layer is evaluated across three backbone architectures: ViT-Tiny [6], MobileNetV3-Large [10], and ResNet-18 [27]. All models are initialized with pre-trained weights from the PyTorch Image Models (timm) library [26] and fine-tuned on each dataset. The NFP module is integrated into each backbone according to the scheme described in Sec. 3.3. In all cases, NFP is placed after the final feature extraction stage, followed by a linear classification head. A  $1 \times 1$  convolution is applied after the NFP to align the number of feature maps from NFP to the average pooled feature maps. This design ensures compatibility with the classifier while maintaining low parameter overhead. Classification is performed by a linear head after multiplying the features of NFP and GAP. The model architectures for each backbone

and pooling variant are trained and evaluated as described above. Results are summarized in Tab. 1.

### 4.3. Overall Comparison

Table 1 compares the proposed NFP against global average pooling (GAP) and recent texture pooling methods (Lacunarity [15], Fractal [7], RADAM [22], and DeepTEN [31]) across five datasets and three backbones. Overall, NFP consistently matches or outperforms the strongest baselines while introducing negligible parameter cost. GAP remains competitive on simpler datasets such as PlantVillage and UC Merced, where nearly all methods achieve accuracies above 98–99%. However, it struggles on texture-heavy domains like GTOS-Mobile, particularly with ViT-Tiny (68.64%), since global averaging discards local structural detail. Texture-aware pooling methods, including NFP, address this limitation by explicitly encoding neighborhood-level relationships.

Handcrafted descriptors such as Lacunarity and Fractal pooling provide modest or inconsistent gains over GAP but are limited by fixed statistical formulations. On ResNet18 with GTOS-Mobile, for instance, Lacunarity improves GAP by just over one percentage point (73.12% vs. 72.01%) but remains below NFP (74.52%). On MobileNetV3, Lacunarity actually underperforms GAP on GTOS-Mobile (73.81% vs. 76.27%) and again falls short compared to NFP (76.49%). These results highlight the inconsistent benefits of handcrafted pooling compared to learnable similarity-based features.

RADAM, which relies on stochastic aggregation of activation maps, can outperform NFP in isolated cases. For example, with MobileNetV3 on UC Merced, RADAM slightly exceeds NFP (98.91% vs. 98.49%). However, this comes at the cost of stability: on GTOS-Mobile, NFP is more reliable, surpassing RADAM by +0.6% (76.49% vs. 75.89%). DeepTEN achieves strong performance on large-scale datasets such as RESISC45, reaching 94.95% with MobileNetV3. Yet these gains come with significant parameter overhead (+1.46M compared to GAP). NFP attains nearly the same accuracy (94.80%) with only +0.09M additional parameters, making it a far more efficient option. On ViT-Tiny with GTOS-Mobile, NFP also surpasses DeepTEN by +5.6% (75.47% vs. 69.84%) despite being significantly lighter. Another advantage of NFP is its robustness. Unlike stochastic approaches such as RADAM, which exhibit high variance across runs (e.g., MobileNetV3 on GTOS-Mobile:  $\pm 3.58$ ), NFP produces stable results with consistently low deviation. This reliability, combined with its lightweight design, makes NFP particularly attractive for real-world deployments where memory footprint and stability are critical.

**Backbone-specific trends.** For CNN-based backbones, NFP provides consistent improvements across datasets, par-

Similarity Measure	Accuracy $\pm$ Std (%)
Cosine	<b>98.86 <math>\pm</math> 0.58</b>
Dot Product	98.25 $\pm$ 0.62
Root Mean Square Error (RMSE)	98.02 $\pm$ 0.56
Sharpened Cosine (SCS)	98.02 $\pm$ 0.79
$L_1$ Norm	98.41 $\pm$ 0.40
$L_2$ Norm	98.25 $\pm$ 0.68
Geman-McClure	97.78 $\pm$ 0.56
Scaled Dot Product	98.10 $\pm$ 0.51
Earth Mover’s Distance (EMD)	98.49 $\pm$ 0.59
Canberra	98.17 $\pm$ 0.59
Hellinger	98.25 $\pm$ 0.56
Chi-Squared Type 1	98.10 $\pm$ 0.34
Chi-Squared Type 2	98.02 $\pm$ 0.49
GFC	98.25 $\pm$ 0.68
Pearson Correlation	97.86 $\pm$ 0.51
Jeffrey Divergence	98.13 $\pm$ 0.58
Squared Chord	98.10 $\pm$ 0.89
Smith Similarity	98.02 $\pm$ 0.98

Table 2. Comparison of similarity measures for NFP using ResNet-18 [27] on the UC Merced dataset [30]. Best average result in **bold**.

ticularly on GTOS-Mobile where texture cues dominate classification. On ResNet18, NFP achieves 74.52%, outperforming Lacunarity (73.12%) and RADAM (69.37%), and shows the highest overall accuracy on UC Merced (98.86%). With MobileNetV3, NFP again delivers the top result on GTOS-Mobile (76.49%), exceeding GAP (76.27%) and clearly surpassing Lacunarity (73.81%). For ViT-Tiny, improvements are smaller on simpler datasets such as PlantVillage and UC Merced but substantial on GTOS-Mobile, where NFP improves over GAP by +6.83%. These results suggest that convolutional backbones benefit most from the neighborhood similarity mechanism, while transformers gain selectively on texture-dominated datasets.

### 4.4. Similarity Measures

A total of 18 similarity metrics are evaluated within the NFP framework using ResNet-18 on the UC Merced dataset to identify the most effective function for capturing local feature relationships. As shown in Tab. 2, cosine similarity achieves the highest classification accuracy (98.86  $\pm$  0.58), emphasizing the importance of angular alignment between feature vectors. This metric captures directional consistency while being invariant to magnitude, making it particularly suitable for remote sensing scenarios with variable illumination and intensity.

Several other metrics, including dot product (98.25  $\pm$  0.62), Hellinger (98.25  $\pm$  0.56), and Earth Mover’s Distance (98.49  $\pm$  0.59), also show strong performance, suggesting

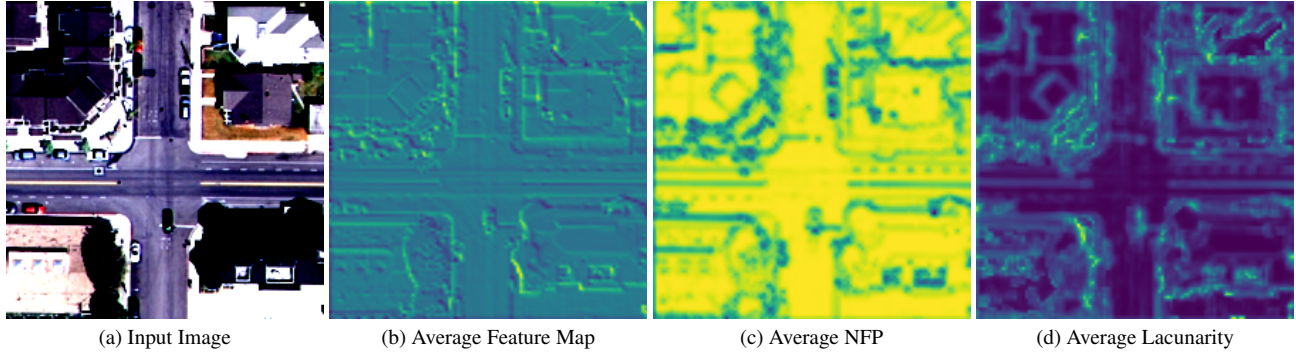


Figure 3. Visualization of feature representations from the first layer of MobileNetV3 [10] on the UC Merced dataset [30], class “intersection.” (b) The standard feature map highlights low-level edges and textures, (c) NFP (cosine similarity) enhances local neighborhood structures, and (d) lacunarity pooling emphasizes spatial gaps and texture distributions. Feature map visualizations are channel-averaged and normalized to the [0,1] range for comparison.

that angle and distribution-aware functions are effective. In contrast, distance-based measures such as root mean square error (RMSE) ( $98.02 \pm 0.56$ ),  $L_1$  norm ( $98.41 \pm 0.40$ ), and  $L_2$  norm ( $98.25 \pm 0.68$ ) result in slightly lower accuracy, indicating that absolute deviations are less informative in texture-based classification tasks. Overall, these results highlight cosine similarity as the most appropriate choice for guiding NFP, due to its ability to preserve fine-grained spatial structure in local neighborhoods.

#### 4.5. Layer Placement

Network Stage	Channels	Acc. $\pm$ Std (%)	Params
Layer 1	16	$98.73 \pm 0.11$	4.24M
Layer 2	24	$98.65 \pm 0.11$	4.24M
Layer 3	40	$98.33 \pm 0.00$	4.24M
Layer 4	112	$98.02 \pm 0.11$	4.25M
Layer 5	960	$98.33 \pm 0.51$	4.31M
All	1152	<b><math>98.89 \pm 0.11</math></b>	4.37M

Table 3. Classification accuracy, number of channels before NFP (cosine similarity), and number of trainable parameters for different insertion stages of MobileNetV3 [10] on UC Merced [30]. Channels are from `features_only` output [26]. Best average result in **bold**.

The effect of inserting the NFP layer at different depths of the backbone is further explored to assess whether early-stage spatial patterns can improve texture-aware classification. Specifically, the MobileNetV3 [10] architecture is evaluated by placing the NFP module after each of its main feature extraction stages (Layers 1 through 5), as defined by the `features_only` outputs of the `timm` library. In each configuration, features from the selected stage are passed through the NFP module, followed by a classification head.

This experimental setup isolates the contribution of each stage’s feature map, enabling a systematic evaluation of where texture information is most beneficial. As summarized in Tab. 3, the highest accuracy is achieved when NFP aggregates features from all stages ( $98.89 \pm 0.11$ ), providing a modest gain over the best single-stage placement. Among individual stages, the strongest result is obtained at Layer 1 ( $98.73 \pm 0.11$ ), with accuracy gradually declining at deeper stages. These results indicate that early-stage features carry strong discriminative texture cues, while multi-stage aggregation further improves performance with a small parameter increase.

Figure 3 demonstrates how NFP modifies early feature representations compared to the baseline backbone. For the “intersection” scene, standard activations highlight edges and coarse textures, whereas NFP emphasizes neighborhood-consistent patterns such as road grids and parcel boundaries. This produces sharper, more spatially coherent responses, indicating that NFP reinforces structural regularities while reducing noisy activations. Such enhanced sensitivity to fine-grained arrangements provides qualitative support for the improvements observed in Tab. 1.

#### 4.6. Explainable AI analysis

To better understand the impact of different pooling strategies on model interpretability, Grad-CAM [23] is employed to visualize class activation maps for models trained with GAP (baseline), NFP, DeepTEN, Fractal, Lacunarity, and RADAM, as summarized in Fig. 4. Including GAP as a baseline enables direct comparison with the widely used global average pooling approach. The GAP model produced attention maps that highlighted regions that are only loosely aligned with the object of interest (airplane in this example). In contrast, NFP yields more semantically relevant activations, accurately localizing critical object parts (such as the airplane fuselage and wings). DeepTEN also

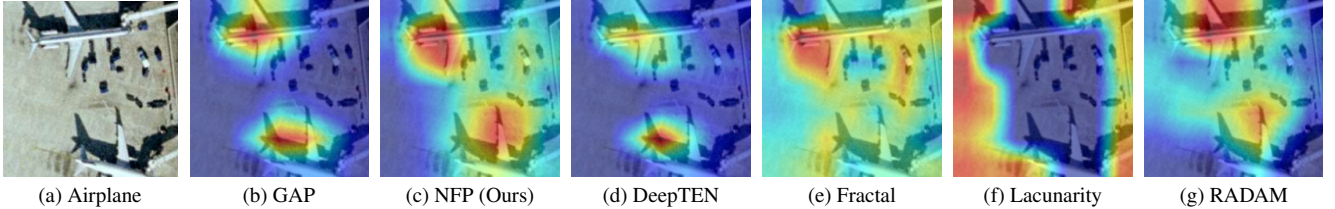


Figure 4. Grad-CAM [23] visualizations for an “Airplane” sample from the UC Merced dataset [30] using MobileNetV3 [10] with different pooling strategies: (a) Original image, (b) GAP (Baseline), (c) NFP (Ours), (d) DeepTEN, (e) Fractal, (f) Lacunarity, and (g) RADAM. Brighter regions indicate higher model attention. NFP consistently yields more focused and semantically meaningful activations, localizing key object regions (e.g., airplane body and wings) better than GAP and other texture pooling methods. These results demonstrate NFP’s superior ability to preserve fine-grained, class-relevant spatial structure.

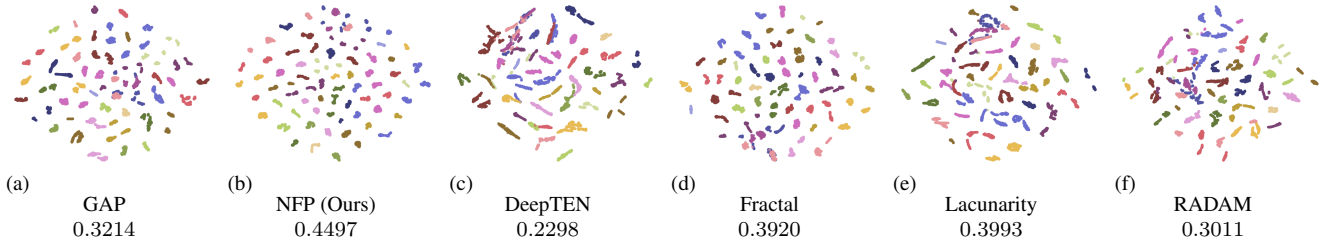


Figure 5. t-SNE visualizations of penultimate-layer features extracted from models trained on GTOS-Mobile (31 classes) with different pooling methods: GAP, NFP (Ours), DeepTEN, Fractal, Lacunarity, and RADAM. Each point represents a test image, colored by ground-truth class. The Silhouette Score (computed on the original feature space) is shown beneath each panel, quantifying the compactness and separability of class clusters. NFP achieves the highest Silhouette Score, indicating its superior ability to produce discriminative and well-separated feature embeddings for texture classification. All runs used a shared random seed for fair comparison.

sharpens attention relative to GAP, but remains more diffuse and less object-centered than NFP. The difference is particularly evident when comparing the concentrated attention in NFP to the more diffuse responses of GAP and RADAM, as well as the less object-aligned focus seen in Fractal and Lacunarity pooling. These results demonstrate that NFP not only improves classification accuracy but also enhances the interpretability of model predictions by producing more meaningful and focused visual explanations.

#### 4.7. t-SNE Visualization Analysis

To evaluate the discriminative power of the learned feature embeddings, penultimate-layer features from each model are visualized using t-distributed Stochastic Neighbor Embedding (t-SNE) [24] on the GTOS-Mobile dataset. Figure 5 presents two-dimensional projections for models utilizing GAP, Fractal, Lacunarity, RADAM, and the proposed NFP. Each point in the scatter plots corresponds to a test sample and different colors correspond to the true class. All visualizations are generated with identical t-SNE hyperparameters and random seed to ensure fair comparisons between models.

In addition to qualitative visual analysis, the Silhouette Score [21] for each method is reported beneath each plot. The Silhouette Score quantifies the compactness and separability of clusters in the original feature space, with higher

values reflecting more well-defined and better-separated class clusters. As summarized in Fig. 5, NFP achieves the highest Silhouette Score (0.4497), indicating the most compact and well-separated clusters among all methods. This result aligns with the visual impression and shows that NFP produces more clearly defined and less overlapping clusters compared to GAP, Fractal, Lacunarity, and RADAM. In contrast, RADAM and GAP show lower Silhouette Scores (0.3011 and 0.3214, respectively), consistent with their more diffuse, overlapping class distributions. In summary, both the qualitative t-SNE visualizations and the quantitative Silhouette Scores demonstrate that NFP enables more discriminative and structured feature embeddings, supporting its superior classification performance on the GTOS-Mobile dataset.

## 5. Conclusion

This work introduces NFP, a method designed to enhance texture-aware classification in remote sensing images. By explicitly modeling local similarity relationships within the feature space, NFP enables convolutional backbones to preserve fine-grained spatial structure alongside global semantic information. Extensive experiments across five public datasets and three backbone architectures demonstrate that NFP consistently matches or surpasses state-of-the-

art pooling methods, including GAP, Lacunarity, Fractal, and RADAM, with up to 6.83% accuracy improvements on challenging benchmarks such as GTOS-Mobile. Importantly, these gains are achieved with minimal additional parameter cost.

Further analyses of similarity metrics, layer placement, and interpretability (e.g., Grad-CAM and t-SNE) confirm that NFP produces more discriminative and semantically meaningful feature embeddings compared to prior methods. Although the largest gains are observed on CNN-based models, NFP also delivers competitive results on transformer-based backbones. Future work include incorporating learnable weighting, radial or multi-scale neighborhoods, parameter-efficient transfer learning, extending NFP toward domain adaptation and lightweight deployment in diverse vision tasks (e.g. object detection and segmentation).

## Acknowledgment

This material is based upon work supported by Texas A&M AgriLife. Portions of this research were conducted with the advanced computing resources provided by Texas A&M High Performance Research Computing. LA-UR-25-30363.

## References

- [1] Faisal Ahmed, Emam Hossain, ASMH Bari, and Md Sakhawat Hossen. Compound local binary pattern (clbp) for rotation invariant texture classification. *International Journal of Computer Applications*, 33(6):5–10, 2011. 1
- [2] Mor Avi-Aharon, Assaf Arbelle, and Tammy Riklin Raviv. Differentiable histogram loss functions for intensity-based image-to-image translation. *IEEE Transactions on Pattern Analysis and Machine Intelligence*, 45(10):11642–11653, 2023. 3
- [3] Gong Cheng, Junwei Han, and Xiaoqiang Lu. Remote sensing image scene classification: Benchmark and state of the art. *Proceedings of the IEEE*, 105(10):1865–1883, 2017. 1, 4
- [4] Gong Cheng, Junwei Han, and Xiaoqiang Lu. Remote sensing image scene classification: Benchmark and state of the art. *Proceedings of the IEEE*, 105(10):1865–1883, 2017. 1
- [5] Hilda Deborah, Noël Richard, and Jon Yngve Hardeberg. A comprehensive evaluation of spectral distance functions and metrics for hyperspectral image processing. *IEEE Journal of Selected Topics in Applied Earth Observations and Remote Sensing*, 8(6):3224–3234, 2015. 3
- [6] Alexey Dosovitskiy, Lucas Beyer, Alexander Kolesnikov, Dirk Weissenborn, Xiaohua Zhai, Thomas Unterthiner, Mostafa Dehghani, Matthias Minderer, Georg Heigold, Sylvain Gelly, et al. An image is worth 16x16 words: Transformers for image recognition at scale. *arXiv preprint arXiv:2010.11929*, 2020. 4
- [7] João B Florindo. Fractal pooling: A new strategy for texture recognition using convolutional neural networks. *Expert Systems with Applications*, 243:122978, 2024. 1, 5
- [8] Pablo Gómez and Gabriele Meoni. Msmatch: Semisupervised multispectral scene classification with few labels. *IEEE Journal of Selected Topics in Applied Earth Observations and Remote Sensing*, 14:11643–11654, 2021. 4
- [9] Zigfried Hampel-Arias and Amanda Ziemann. Experiments in anomalous change detection: Improving detector discrimination through feature layers. In *Algorithms, Technologies, and Applications for Multispectral and Hyperspectral Imaging XXIX, Proc. SPIE*, page 125190P, 2023. 2
- [10] Andrew Howard, Mark Sandler, Grace Chu, Liang-Chieh Chen, Bo Chen, Mingxing Tan, Weijun Wang, Yukun Zhu, Ruoming Pang, Vijay Vasudevan, et al. Searching for mobilenetv3. In *Proceedings of the IEEE/CVF International Conference on Computer Vision (ICCV)*, pages 1314–1324, 2019. 3, 4, 6, 7
- [11] David Hughes, Marcel Salathé, et al. An open access repository of images on plant health to enable the development of mobile disease diagnostics. *arXiv preprint arXiv:1511.08060*, 2015. 4
- [12] J. T. Kerr and M. Ostrovsky. From space to species: Ecological applications of remote sensing. *Trends in Ecology & Evolution*, 18(6):299–305, 2003. 1
- [13] Ying Li, Haokui Zhang, Xizhe Xue, Yenan Jiang, and Qiang Shen. Deep learning for remote sensing image classification: A survey. *Wiley Interdisciplinary Reviews: Data Mining and Knowledge Discovery*, 8(6):e1264, 2018. 1
- [14] Biyang Liu, Huimin Yu, and Yangqi Long. Local similarity pattern and cost self-reassembling for deep stereo matching networks. In *Proceedings of the AAAI Conference on Artificial Intelligence*, pages 1647–1654, 2022. 2
- [15] Akshatha Mohan and Joshua Peebles. Lacunarity pooling layers for plant image classification using texture analysis. In *Proceedings of the IEEE/CVF Conference on Computer Vision and Pattern Recognition (CVPR) Workshops*, pages 5384–5392, 2024. 1, 5
- [16] David J. Mulla. Twenty five years of remote sensing in precision agriculture: Key advances and remaining knowledge gaps. *Biosystems Engineering*, 114(4):358–371, 2013. 1
- [17] Maxim Neumann, André Susano Pinto, Xiaohua Zhai, and Neil Houlsby. In-domain representation learning for remote sensing. *arXiv preprint arXiv:1911.06721*, 2019. 4
- [18] Timo Ojala, Matti Pietikäinen, and David Harwood. Performance evaluation of texture measures with classification based on kullback discrimination of distributions. In *Proceedings of the 12th International Conference on Pattern Recognition (ICPR)*, pages 582–585. IEEE, 1994. 1
- [19] Joshua Peebles, Weihuang Xu, and Alina Zare. Histogram layers for texture analysis. *IEEE Transactions on Artificial Intelligence*, 3(4):541–552, 2021. 1
- [20] Anne Puissant, Jacky Hirsch, and Christiane Weber. The utility of texture analysis to improve per-pixel classification for high to very high spatial resolution imagery. *International Journal of Remote Sensing*, 26(4):733–745, 2005. 1

[21] Peter J. Rousseeuw. Silhouettes: A graphical aid to the interpretation and validation of cluster analysis. *Journal of Computational and Applied Mathematics*, 20:53–65, 1987. [7](#)

[22] Leonardo Scabini, Kallil M Zielinski, Lucas C Ribas, Wesley N Gonçalves, Bernard De Baets, and Odemir M Bruno. Radam: Texture recognition through randomized aggregated encoding of deep activation maps. *Pattern Recognition*, 143:109802, 2023. [1](#), [5](#)

[23] Ramprasaath R. Selvaraju, Michael Cogswell, Abhishek Das, Ramakrishna Vedantam, Devi Parikh, and Dhruv Batra. Grad-cam: Visual explanations from deep networks via gradient-based localization. In *Proceedings of the IEEE International Conference on Computer Vision (ICCV)*, pages 618–626, 2017. [6](#), [7](#)

[24] Laurens Van der Maaten and Geoffrey Hinton. Visualizing data using t-sne. *Journal of Machine Learning Research*, 9 (Nov):2579–2605, 2008. [7](#)

[25] Thilo Wellmann, Angela Lausch, Erik Andersson, et al. Remote sensing in urban planning: Contributions towards ecologically sound policies? *Landscape and Urban Planning*, 204:103921, 2020. [1](#)

[26] Ross Wightman. Pytorch image models. <https://github.com/rwightman/pytorch-image-models>, 2019. Accessed: 2025-08-17. [4](#), [6](#)

[27] Ross Wightman, Hugo Touvron, and Hervé Jégou. Resnet strikes back: An improved training procedure in timm. *CoRR*, abs/2110.00476, 2021. [4](#), [5](#)

[28] Skyler Wu, Fred Lu, Edward Raff, and James Holt. Exploring the sharpened cosine similarity. *arXiv preprint arXiv:2307.13855*, 2023. [3](#)

[29] Jia Xue, Hang Zhang, and Kristin Dana. Deep texture manifold for ground terrain recognition. In *Proceedings of the IEEE Conference on Computer Vision and Pattern Recognition (CVPR)*, pages 558–567, 2018. [4](#)

[30] Yi Yang and Shawn D. Newsam. Bag-of-visual-words and spatial extensions for land-use classification. In *Proceedings of the 18th ACM SIGSPATIAL International Conference on Advances in Geographic Information Systems (GIS)*, pages 270–279, 2010. [1](#), [4](#), [5](#), [6](#), [7](#)

[31] Hang Zhang, Jia Xue, and Kristin Dana. Deepten: Texture encoding network. In *Proceedings of the IEEE Conference on Computer Vision and Pattern Recognition (CVPR)*, pages 708–717, 2017. [1](#), [5](#)

[32] Liangpei Zhang, Lefei Zhang, and Bo Du. Deep learning for remote sensing data: A technical tutorial on the state of the art. *IEEE Geoscience and Remote Sensing Magazine*, 4(2):22–40, 2016. [1](#)

[33] L. Zhao et al. An improved pooling method for convolutional neural networks. *Scientific Reports*, 2024. max pooling loses positional information; average pooling loses fine details. [1](#)